The Astronomical Journal, 123:1776–1783, 2002 March

ASTROMETRY AND NEAR-INFRARED PHOTOMETRY OF NEPTUNE'S INNER SATELLITES AND RING ARCS

Christophe Dumas and Richard J. Terrile
Jet Propulsion Laboratory, Mail Stop 183-501, California Institute of Technology, 4800 Oak Grove Drive, Pasadena, CA 91109

Bradford A. Smith
Institute for Astronomy, University of Hawaii, 2680 Woodlawn Drive, Honolulu, HI 96822

and

Glenn Schneider
Steward Observatory, University of Arizona, 933 North Cherry Avenue, Tucson, AZ 85721
Received 2001 August 8; accepted 2001 December 6

ABSTRACT

We report 1.87 μm photometry and astrometry of the inner satellites (Proteus, Larissa, Galatea, and Despina) and ring arcs of Neptune, obtained with the *Hubble Space Telescope* and its near-infrared camera NICMOS. From comparison with the *Voyager* data obtained at visible wavelengths, the small bodies orbiting within the ring region of Neptune have a near-infrared albedo consistently low, but higher than at visible wavelengths for most of the satellites, ranging from $p_{1.87\ \mu m} = 0.058$ (Despina) to $p_{1.87\ \mu m} = 0.094$ (Proteus). The ring arcs display a reddish spectral response similar to the satellites' in the 0.5–1.9 μm wavelength range. If we consider an earlier photometric measurement of Proteus obtained at K band, the satellite's albedo shows a depression at 2.2 μm that could be the first spectral evidence for the presence of C—H or C≡N bearing material on its surface. Although astrometry of the inner moons of Neptune yields positions consistent with the predictions derived from *Voyager* images, the long time base between the *Voyager* and NICMOS observations allows us to refine our knowledge of their mean motions and semimajor axes, and to decrease the errors associated with these measurements. In addition, we confirm a mismatch between the mean semimajor axis of the ring arcs and the location of the 42 : 43 corotation inclined resonance due to Galatea. This result calls into question the ability of this resonance to confine the arcs azimuthally.

Key words: astrometry — planets and satellites: individual (Neptune) — techniques: photometric

1. INTRODUCTION

The inner system of Neptune was imaged for the first time in 1989 by *Voyager* (Smith et al. 1989). The images collected during the flyby revealed a system of small moons and rings displaying a low albedo at visible wavelengths (Thomas & Veverka 1991). Prior to the *Voyager* encounter, observers had reported a system of incomplete arcs from stellar occultation events (Hubbard et al. 1986). Because of their small optical depth (Horn et al. 1990), the rings of Neptune could not be observed from Earth, and only the ring arcs, which orbit inside the Adams ring, are sufficiently dense (optical depth ~10 times larger than the rings) to be detected from stellar occultation. Because the rings and small satellites of Neptune are faint ($V_{mag} \sim 20$–25) and orbit at only a few Neptunian radii (R_N) from the planet's center ($2R_N$–$5R_N$), their detection from Earth's vicinity is particularly challenging. For this reason, only a few direct observations of the inner Neptunian system were carried out over the past decade: Proteus was first detected in the visible (Colas & Buil 1992) and then at K band from adaptive optics observations (Roddier et al. 1997), while images of the small satellites Proteus, Larissa, Galatea, and Despina were obtained from space at visible wavelengths with the *Hubble Space Telescope* (*HST*) (Pascu et al. 1999). Because of this limited data set, our study of the inner system of Neptune was, until recently, mostly based on the visible images collected by *Voyager*. The observational breakthrough came in the late '90s with the availability of sensitive near-infrared cameras and diffraction-limited telescopes that could return subarcsecond angular resolution (Dumas et al. 1999; Sicardy et al. 1999). The near-infrared range is particularly well suited to study of Neptune's inner system, since it allows the observations to be carried out through the absorption bands of the gaseous methane present in the planet's atmosphere, which considerably decreases the scattered-light contamination and therefore returns higher contrast images of the satellites and rings. This wavelength range also provides a better investigation of the surface composition of these planetary bodies, since most of the ices, organics, and minerals have their low-overtone and combination absorption bands in this spectral region.

In many respects, the Uranian and Neptunian systems of rings and small moons are very similar. Both planets display a system of thin rings confined by resonance with small nearby satellites (diameters from 20 to 200 km) whose surfaces appear to be covered with dark ($p_{vis} \sim 0.06$–0.07), possibly organics-rich material (Thomas, Weitz, & Veverka 1989; Thomas & Veverka 1991). More recent observations of Uranus's inner moons by the *HST* Wide Field Planetary Camera 2 (WFPC2) (Karkoschka 1997) returned a revised visible albedo for the small moon Puck ($p_{vis} \sim 0.1$) slightly higher than the *Voyager* estimate, but still within the typical range of albedos for small outer solar system bodies. The particularity of Neptune's system of rings lies within its dynamically stable ring arcs. After the discovery by *Voyager* of the inner satellite Galatea, orbiting interior to the ring arcs on a slightly inclined orbit (Owen, Vaughan, & Synnott 1991), and based on the corotation model developed by Goldreich, Tremaine, & Borderies (1986), Porco (1991)

showed that Galatea could create both the Lindblad resonance and corotation inclined resonance (CIR) that could respectively confine the arcs radially and azimuthally. Because of uncertainty as to which specific arcs occulted the background stars during the stellar occultation events observed in 1984 and later (Hubbard et al. 1986), two solutions for the ring arcs' mean motion were obtained by Nicholson, Mosqueira, & Matthews (1995), but only one of these solutions was generally considered because it positioned the ring arcs closer to the center of the CIR than the other.

Here we report photometric and astrometric measurements obtained from a complete analysis of the observations of Neptune carried out with *HST* and its Near Infrared Camera and Multi-Object Spectrometer (NICMOS) on 1998 October 20 and 22. These new measurements take into account the small difference in pixel scale along the vertical and horizontal axes of the camera and confirm, without ambiguity, the mismatch between the position of the ring arcs and the location of the 42 : 43 CIR with Galatea (Dumas et al. 1999; Sicardy et al. 1999).

2. OBSERVATIONS

NICMOS has three 256 × 256 low-noise HgCdTe detectors sensitive in the 0.8–2.5 μm range (Thompson et al. 1998). We used NICMOS camera 2 (NIC2; $19\farcs46 \times 19\farcs28$ field of view) to image the Neptunian system of small moons and ring arcs on 1998 October 20 and 22 (*HST* guaranteed time observer [GTO] program 7244). For these dates, Neptune's phase and ring opening angles were $1\fdg9$ and $-27°$, respectively. The NIC2 F187W filter (central wavelength 1.8722 μm, FWHM = 0.2436 μm) was employed to aid in the rejection of background light. The filter bandpass corresponds to a strong absorption in the spectrum of methane, a major constituent in Neptune's atmosphere. The resolution obtained with NIC2 is $3\fdg2$ per resolution element ($1\fdg6$ pixel^{-1}) at the distance of the ring arcs, which corresponds to an angular resolution of 3500 km along the Adams ring (in which the arcs are embedded). During each visit, the images were acquired while Neptune's disk ($2\farcs36$ diameter) was entirely on the detector, its center positioned at about $7''$ from the *X*-edge of the detector, and a dithering pattern (11 positions, $1\farcs246$ steps) along the *Y*-axis of the detector was employed to record 11 exposures of 208 s each (MULTIACCUM mode, STEP16, NSAMP = 19). This configuration allowed us to generate, for each date, a synthetic image of the distribution of Neptune's scattered light (see § 3 below). Such relatively short exposures of Neptune's inner region were required in order to prevent the small moons and ring arcs from being smeared in a single image as a result of their own orbital motion (Proteus's and Despina's orbital motions during a single 45 minute *HST* visit are respectively $10°$ and $33°$). The detection of the ring arcs was secured by scheduling the observations near maximum of elongation (beginning of sequence at 1229 UT and 1742 UT for October 20 and 22, respectively).

3. DATA REDUCTION

We used the calibrated images delivered by the STScI pipeline; the only modifications made on the CALNICA-processed frames were to correct them for (1) the bias differences between the four camera quadrants (this task was done prior to applying the flat field) and (2) the remaining bad pixels. We then resampled all the images by a factor of 2 onto a finer grid and co-registered them using bicubic convolution interpolation (Park & Schowengerdt 1983) in order to obtain a cube of images centered on Neptune. The small difference in pixel scale along the horizontal and vertical axes of the detector was taken into account ($0\farcs0760$ pixel^{-1} in *X*, $0\farcs0753$ pixel^{-1} in *Y*), and a precision of 0.02 pixels ($\sim$1.5 mas) was achieved during the co-registration process by minimizing the difference in the diffraction pattern of Neptune in adjacent images. The immediate benefit of these manipulations was to improve the final spatial resolution of our images so that the measurement error of the arcs' position along the Adams ring was reduced to $\pm1°$.

In order to obtain a model of the planet's scattered light, we first masked the contribution of the satellites and estimated the flux distribution in the masked regions using a smooth surface fitting interpolation (Akima 1978). For each date, a model of Neptune's scattered light was created so that each pixel value corresponded to the median across the 11 recentered images. The models were then subtracted from the images in order to (1) recover a background level close to zero at the distance of the arcs from Neptune's center and (2) eliminate stray light produced by the secondary-mirror support structure. This step was crucial because, as a result of strong constraints on the orientation of *HST*, it was not possible to position the diffraction spikes away from the point of maximum elongation of the arcs, forcing them to cross an area of high background during the two *HST* visits. Figure 1 shows the satellites Proteus, Larissa, and Galatea as imaged by NICMOS on 1998 October 22, after removing the scattered light produced by Neptune. The physical center point of the Neptunian system was determined for each date by fitting the orbital motion of the inner moons and using the satellite pole solutions derived by Owen et al. (1991). In the case of the ring arcs, the flux from the brightest arcs, Egalité and Fraternité (0.065 μJy pixel^{-1}), was just above the noise level in the individual images. A higher contrast (Fig. 2) was achieved by adding up the individual frames after compensating for the orbital motion of the ring arcs and reprojecting the images into Neptune's equatorial plane (J2000 pole solution for Neptune: R.A. = $299\fdg33$, decl. = $42\fdg94$; Jacobson et al. 1990—not corrected for precession due to Triton).

4. DISCUSSION

4.1. *Satellites*

The revised mean motion and semimajor axes of Neptune's inner satellites Proteus, Larissa, Galatea, and Despina are reported in Table 1. Most of the satellites were found at positions a few degrees ahead of their predicted orbital locations, except for Despina, which was found $\sim4°$ behind. In any case, the offsets are, for all satellites, within the error of the predictions made from the *Voyager* measurements (Owen et al. 1991), and the revised values of the satellites' mean motions differ only by less than $0\fdg002$ day^{-1} from the 1989 determinations. Similar results on the astrometry of the inner satellites of Neptune have been reported from a preliminary analysis of *HST* WFPC2 images by Pascu et al. (1999).

Table 2 lists the 1.87 μm photometric measurements made for each of Neptune's satellites detected by NICMOS

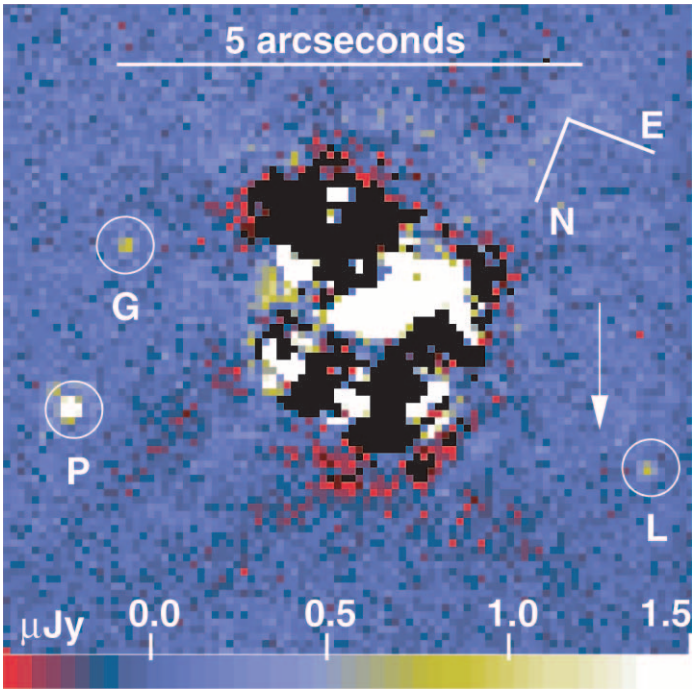

FIG. 1.—Single image of the Neptunian system of small satellites after subtraction of a model of Neptune's scattered light. The image was recorded by NICMOS on 1998 October 22 at 1742 UT (MJD = 51,108.73764746), using the F187W filter, whose bandpass corresponds to a strong absorption of Neptune's atmospheric methane. Proteus (P), Larissa (L), and Galatea (G) are recovered after subtraction of the scattered-light model. Despina was located in the proximity of Neptune's south pole and could not be detected on that date. The arrow points to the location of the ring arcs of Neptune. The black-and-white region in the center of the image corresponds to the residual flux after subtraction of the light produced by Neptune (scattered-light model). The scale bar at the bottom of the image represents the flux in microjanskys per pixel. The angular scale and camera orientation are also shown at the top of the figure.

(Proteus, Larissa, Galatea, and Despina). A 5×5 pixel photometric aperture was used to encircle the energy of all the satellites except Proteus (11×11 square), which is $\sim$10 times brighter than Larissa and Galatea in our images. We then generated a synthetic F187W NIC2 point-spread function using Tiny Tim (Krist & Hook 1997) to estimate the amount of flux neglected by the use of small apertures and corrected our measurements accordingly. The innermost moons, Thalassa and Naiad, could not be detected because of their small size (estimated diameters of 40 and 29 km, respectively; Thomas & Veverka 1991) and small semimajor axes ($a \sim 2R_N$). We used the solar flux given by Labs & Neckel (1968) and satellite radii determined from the *Voyager* data (Thomas & Veverka 1991) to derive the geometric albedo of the small Neptunian moons. Our images lead to 1.87 μm magnitudes ranging from $\sim$18.3 (Proteus) to $\sim$21.1 (Despina). No correction to zero phase angle has been made to the NICMOS measurements, because the phase coefficient β of the satellites' surfaces is not known at near-infrared wavelengths, and also because our observations were obtained at low phase angle, so this correction would be negligible. We note that the error on Galatea's albedo is too large to derive a meaningful color of this object. The larger dispersion of Galatea's photometric points might be

TABLE 1
REVISED MEAN MOTION AND SEMIMAJOR AXES FOR NEPTUNE'S INNER SATELLITES AND RING ARCS

Name	$\Delta_{long.}$[a] (deg)	Mean Motion (deg day^{-1})	Mean Semimajor Axis (km)
Proteus	+0.6 ± 0.2 (3.0)	320.7656 ± 0.0001 *(320.7654)*	117,647.19 ± 0.04 *(117,647.11)*
Larissa	+1.5 ± 0.5 (5.4)	649.0539 ± 0.0001 *(649.0534)*	73,548.32 ± 0.03 *(73,548.33)*
Galatea	+5.7 ± 1.2 (8.4)	839.6615 ± 0.0004 *(839.6598)*	61,952.60 ± 0.03 *(61,952.67)*
Despina	−4.0 ± 1.5 (9.4)	1075.7330 ± 0.0004 *(1075.7342)*	52,525.99 ± 0.03 *(52,525.95)*
Ring arcs.....	+1.5 ± 1.0[b] (2.0)[c]	820.1122 ± 0.0003 *(820.1118)*[c]	62,932.70 ± 0.03 *(62,932.72)*[c]

NOTE.—Numbers in italics refer to measurements from the *Voyager* era: Owen et al. 1991 for the satellites, and Nicholson et al. 1995 for the ring arcs.

[a] The $\Delta_{long.}$ measurements refer to the longitude offset with respect to the predicted orbital positions of the satellites. The numbers in parentheses are the integrated uncertainties of the *Voyager* ephemerides.

[b] The offset in orbital position of the ring arcs is measured with respect to the predicted position of the middle of the arc Egalité using $n = 820.^{\circ}1118$ day^{-1} (solution 2) for the ring arcs' mean motion (Nicholson et al. 1995).

[c] The number in parentheses corresponds to solution 2 ($n_2 = 820.^{\circ}1118$ day^{-1}) for the arcs' mean motion, whereas solution 1 ($n_1 = 820.^{\circ}1194$ day^{-1}) was preferred prior to the 1998 observations. Solution 1 corresponds to a mean semimajor axis $a_1 = 62{,}932.33$ km, and solution 2 to $a_2 = 62{,}932.72$ km (see § 4.3 and Dumas et al. 1999 for additional discussion).

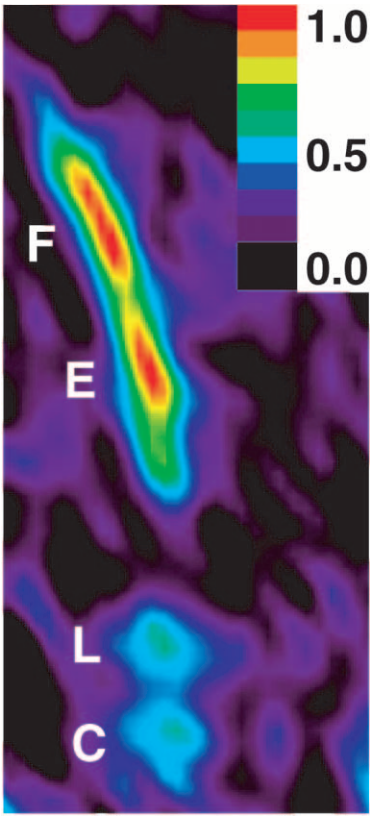

FIG. 2.—False-color image of the four ring arcs of Neptune, Courage, Liberté, Egalité, and Fraternité (from leading to trailing) obtained after co-registering the 22 dithered images obtained with NICMOS on 1998 October 20 and 22 (Dumas et al. 1999). The image has been reprojected as an observer would look at the arcs from the southern ring-plane normal. The color has been scaled so that the brightest arc has a value of unity.

due both to the uncertainties in the determination of the background level at this small angular distance from Neptune and to possible variations of the apparent cross section and local albedo of Galatea for the two different orbital positions observed with NICMOS.

Figure 3 is a compilation of the photometric data set obtained to date on Neptune's inner satellites (including the ring arcs, which will be discussed in § 4.3). At visible wavelengths, the satellites and ring arcs display similar albedos, all being distributed around $p \sim 0.06$ (Thomas & Veverka 1991). The albedo distribution is slightly more dispersed at 1.87 μm, with values ranging from $p = 0.058 \pm 0.036$ (Despina) to $p = 0.094 \pm 0.011$ (Proteus), although we can conclude that, within the error of our measurements, the ring arcs and all the satellites have a red-to-neutral color. This color trend is typical of the colors for the dark asteroids (Dumas, Owen, & Barucci 1998) and indicates that their surfaces might be covered with dark, "primitive" material (see § 4.2). An additional ground-based measurement of Proteus's geometric albedo at 2.2 μm ($p_K = 0.058 \pm 0.016$) obtained with adaptive optics at the Canada-France-Hawaii Telescope (CFHT) (Roddier et al. 1997) is also plotted in Figure 3. Analysis of the rotation of the surface features found on Proteus by *Voyager* (Thomas & Veverka 1991) supports a synchronous rotation of the satellite around Neptune, and we determined that the sub-Earth longitude of Proteus (180°) at the time of the CFHT observations (1995 August 12, 1038 UT; MJD = 49,941.44306) was very close to the longitude at the time of the NICMOS observations (208° on 1998 October 20, 1229 UT [MJD = 51,106.52014], and 214° on 1998 October 22, 1742 UT [MJD = 51,108.73750]). Therefore, any wavelength variation of Proteus's albedo between these two independent observations should be due to the nature of the chemical compounds present on the surface, rather than changes in the apparent diameter or local albedo distribution of the satellite.

TABLE 2
1.87 μm NICMOS PHOTOMETRY OF NEPTUNE'S INNER SATELLITES AND RING ARCS

Name	Flux[a] (μJy)	1.87 μm Magnitude[b]	$p_{1.87\ \mu m}$[c]	$p_{0.48\ \mu m}$[d]
Proteus	38.08 ± 2.68	18.34 ± 0.08	0.094 ± 0.011	0.061
Larissa	6.78 ± 0.91	20.22 ± 0.16	0.079 ± 0.022	0.056
Galatea	5.01 ± 2.04	20.54 ± 0.57	0.086 ± 0.061	0.063
Despina	2.96 ± 1.05	21.12 ± 0.47	0.058 ± 0.036	0.059
Ring arcs[e].....	4.66 ± 0.71	20.63 ± 0.18	0.083 ± 0.012	0.055

NOTE.—F187W NICMOS camera 2 filter: $\lambda_{eff} = 1.871$ μm; FWHM = 0.244 μm.

[a] Inverse sensitivity = 3.819×10^{-6} Jy s ADU^{-1}.

[b] F187W zero-magnitude point = 828 Jy (uncertainty of ±1%).

[c] The geometric albedos are derived using the radii of Neptune's satellites measured by *Voyager*: $R_{Proteus} = 208 \pm 5$ km; $R_{Larissa} = 96 \pm 7$ km; $R_{Galatea} = 79 \pm 12$ km; $R_{Despina} = 74 \pm 10$ km (Thomas & Veverka 1991).

[d] Albedo values (Thomas & Veverka 1991) for the *Voyager* "clear" filter ($\lambda_{eff} = 0.48$ μm; FWHM = 0.19 μm).

[e] For the ring arcs, we refer to the total integrated flux and its corresponding magnitude at 1.87 μm.

4.2. *Proteus*

The chemical nature of the species responsible for both the red slope of Proteus's albedo displayed at shorter wavelengths and the drop in reflectance beyond 2.0 μm cannot be assessed from the crude spectrophotometric study (three independent measurements in the 0.5–2.5 μm range) presented in this paper. Nevertheless, recent analysis of additional near-infrared photometric observations of Proteus (*HST*/NICMOS GTO program 7182) confirms the spectral behavior of Proteus's surface (Dumas et al. 2001), justifying a preliminary attempt to identify the possible chemical compound or compounds responsible. Because water ice covers the surface of most of the satellites of the outer planets, it is also expected to be present on, or near, the surface of the inner moons of Neptune. Unfortunately, the NICMOS F187W and ground-based *K*-band filters cannot be used to efficiently test for the presence of surface water ice, since their bandpasses cover spectral regions that are both inside and outside the absorption bands of water. Also, it is important to note that the reddish slope displayed by Proteus (and the other inner moons of Neptune in general) between visible and near-infrared wavelengths cannot simply be produced by water ice, the reflectance spectrum of which is blue at these wavelengths, but is more likely to be the result of energetic processing of the material originally present on the surface. UV photolysis or energetic-particle bombardment of a mixture of water with carbon-rich and nitrogen-rich compounds can produce complex organic material (Sagan & Khare 1979), and this process might be responsible for the red-to-neutral spectral slope and low surface albedo of the primitive objects that populate the outer

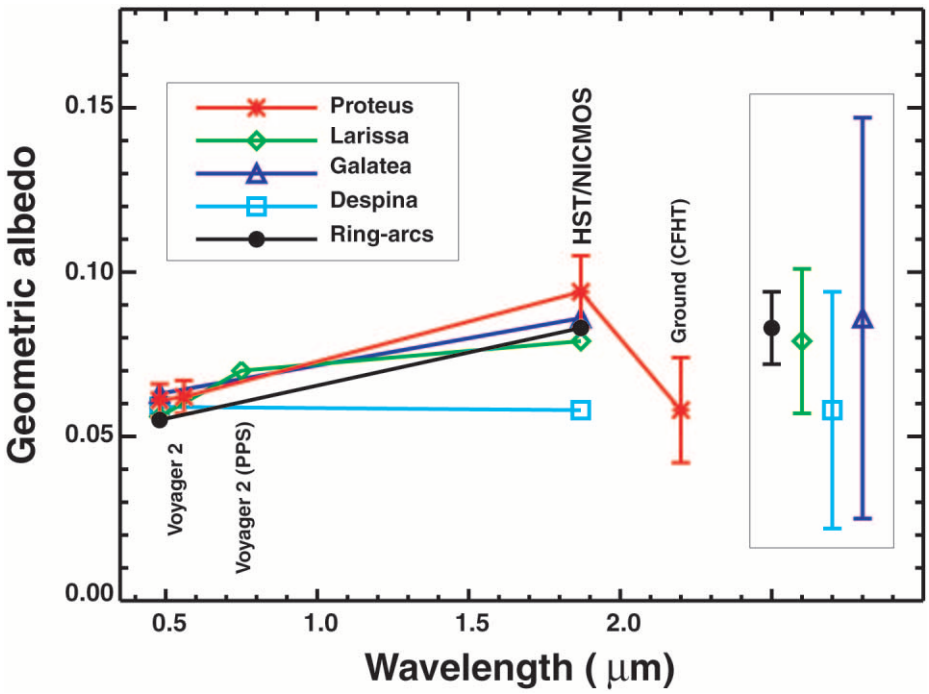

FIG. 3.—Geometric albedo of four of the inner satellites of Neptune (Proteus, Larissa, Galatea, and Despina) and of the ring arcs obtained at 1.87 μm with NICMOS. Measurements at visible wavelengths (0.48, 0.56, 0.75 μm) from *Voyager* (Thomas & Veverka 1991; Lane et al. 1989) and at *K* band ($p_K = 0.058 \pm 0.016$) from the ground (Roddier et al. 1997) are also reported. The near-infrared observations carried out with NICMOS show that the reddish color of the ring arcs is identical to the average color displayed by the small satellites, suggesting a similar composition. Although a higher spectral resolution is required to obtain a meaningful compositional diagnostic of Proteus's surface, material bearing C—H or C≡N could produce the drop in albedo beyond 2.0 μm. Note that to improve the clarity of the figure, the 1.87 μm measurements of Larissa, Galatea, Despina, and the ring arcs have been separately duplicated with their error bars on the right side of the figure.

regions of the solar system. Both the low albedo and the reddish spectral slope of Neptune's inner moons are consistent with the possible presence of organic-rich material on the surface, and material bearing either C—H or C≡N could create the albedo drop measured beyond 2.0 μm for Proteus. In any case, additional spectrophotometric data on Neptune's inner satellites need to be collected using a combination of high angular resolution and near-infrared spectrophotometry to ascertain the nature of the chemical compounds on their surfaces.

We note that the high-contrast, diffraction-limited photometric measurements of Proteus obtained with NICMOS disagree with seeing-limited observations obtained with the coronagraph "CoCo" at the NASA Infrared Telescope Facility. Trilling & Brown (2000) reported surprisingly low *J*- and *H*-band albedo values for Proteus ($p_J \sim 0.026 \pm 0.005$, $p_H \sim 0.028 \pm 0.006$) when compared with the data shown in Figure 3. Although the CoCo data (longitude 95° for 1999 September 8, 0903 UT; MJD = 51,429.37708) were obtained while Proteus was located ~120° away from the orbital position corresponding to the NICMOS images, the nearly homogenous distribution of surface albedo and nearly regular shape of Proteus measured by *Voyager* (Thomas & Veverka 1991) appear incompatible with the albedo discrepancy reported between the NICMOS and CoCo observations. In addition, the low CoCo albedos are difficult to conciliate with the 6% albedo reported by *Voyager* at 0.5 μm. Instead, we suggest that the CoCo photometric measurements could suffer from a poor estimation of the scattered light produced by the planet, in particular at the *J* and *H* bands, where Neptune's scattered light is very strong, or from inaccuracy in the absolute photometric calibration. This statement appears to be supported by the similar discrepancy found between the CoCo *J*- and *H*-band albedos derived for the Uranian satellites Puck, Portia, and Rosalind and the measurements obtained by Karkoschka (2001) using WFPC2 and NICMOS on *HST*.

4.3. *Ring Arcs*

The data reduction process described earlier led to the rediscovery of the four ring arcs of Neptune, which are shown in Figure 2 reprojected as seen by an observer normal to the ring plane. Following the practice employed in earlier studies of Neptune's rings (Smith et al. 1989; Porco et al. 1995), we define $E_i(\lambda) = \mu \int I(\lambda)/F(\lambda) dr$ as the equivalent width, where $I(\lambda)$ is the observed flux reflected from the arcs, $\pi F(\lambda)$ is the incident solar flux, λ is the effective wavelength, and μ is the cosine of the emission angle with respect to the ring-plane normal. In the optically thin case, which includes all of the ring arcs, we can express the equivalent width as $E_i(\lambda) = \frac{1}{4}\langle \varpi(\lambda) P(\phi) \rangle \int \tau \, dr$, where $\varpi(\lambda)$ is the single-scattering albedo, $P(\phi)$ is the phase function, ϕ is the phase angle, and τ is the optical depth of small and large particles (although in backscattered light, the brightness of the ring is primarily determined by the large particles). If we assume that the optical depth of Egalité has remained unchanged since 1989, and if we neglect the correction to zero phase angle ($\phi_{\rm obs} \sim 1\overset{\circ}{.}9$), then the equivalent width seen by NICMOS, $E_i \sim 78 \pm 12$ m, implies a ring-arc geometric albedo $p_{1.87\,\mu{\rm m}} = 0.083 \pm 0.012$, which needs to be compared with the visible geometric albedo obtained from *Voyager* ($p_{0.5\,\mu{\rm m}} = 0.055 \pm 0.004$; Porco et al. 1995). We note

that our revised value for the arcs' albedo is slightly larger than that reported earlier by Dumas et al. (1999), since it now reflects a photometric correction made to the NICMOS measurements to take into account the small apertures used in the photometric analysis. The total integrated flux for all of the arcs is 4.66 ± 0.71 μJy, which corresponds to a near-infrared magnitude $m_{1.87\,\mu\mathrm{m}} = 20.6 \pm 0.2$ (Table 2).

Our reanalysis of the astrometry of the satellites and ring arcs (Table 1) confirms the previous results reported by Dumas et al. (1999) and Sicardy et al. (1999), which showed that the mean semimajor axis of the ring arcs is not located precisely at the 42 : 43 corotation inclined resonance with Galatea. As mentioned in § 1, two possible solutions, n_1 ($820\overset{\circ}{.}1194 \pm 0\overset{\circ}{.}006$ day^{-1}) and n_2 ($820\overset{\circ}{.}1118 \pm 0\overset{\circ}{.}006$ day^{-1}), for the ring arcs' mean motion were derived by combining the *Voyager* and stellar occultation data (Nicholson et al. 1995). The corresponding mean semimajor axes for the ring arcs are $a_1 = 62932.33$ km and $a_2 = 62932.72$ km, respectively. Until recently, solution n_1 for the ring arcs' mean motion was preferred because it positioned the ring arcs closer to the center of the CIR than did solution n_2 (160 m away for n_1, 230 m for n_2). Thanks to the $\sim$9 yr time lag between the *Voyager* and NICMOS observations, the difference between the two possible solutions n_1 and n_2 translated into a $\sim 25^\circ$ mismatch for the ring arcs' orbital location. Using the middle of Egalité as fiducial, we measured the location of the ring arcs in our images and derived a longitude of 354° for Egalité for the date corresponding to the first NICMOS exposure (1998 October 20 at 1229 UT), which corresponds to an arc location $\sim 23\overset{\circ}{.}5$ behind the position predicted for solution n_1 (only $1\overset{\circ}{.}5$ ahead of the position corresponding to solution n_2). The revised value for the arcs' mean motion is therefore $n_{\mathrm{arcs}} = 820\overset{\circ}{.}1122 \pm 0\overset{\circ}{.}003$ day^{-1} (Table 1).

From the CIR model described by Goldreich et al. (1986), the 42 : 43 CIR with Galatea could create 86 ($2m_C$ with $m_C = 43$, the wavenumber associated with the CIR) equally spaced libration sites around Neptune, each of them being potentially capable of azimuthally confining the dust within the Adams ring to form a stable arc. The relation between the mean motion of Galatea n_{G} and the CIR mean motion n_C is expressed as

$$m_C n_C = (m_C - 1) n_{\mathrm{G}} + \dot{\Omega} \, ,$$

where $\dot{\Omega}$ is Galatea's nodal precession rate. For large values of m_C, each corotation resonance is located near a Lindblad resonance (LR) produced by the same satellite, and the relation between the mean motion of Galatea and the LR mean motion n_{L} is

$$m_{\mathrm{L}} n_{\mathrm{G}} = (m_{\mathrm{L}} + 1) n_{\mathrm{L}} - \dot{\omega} \, ,$$

where $\dot{\omega}$ is the arc's apsidal precession rate and m_{L} is the LR wavenumber (which must differ from the corotation wavenumber by ± 1; in the present case, the best match is obtained for $m_{\mathrm{L}} = 42$). Using the NICMOS determination of n_{G} ($839\overset{\circ}{.}6615 \pm 0\overset{\circ}{.}004$ day^{-1}) from Table 1, and the values of $\dot{\Omega} = -0\overset{\circ}{.}714836$ day^{-1} and $\dot{\omega} = 0\overset{\circ}{.}6772$ day^{-1} calculated by Owen et al. (1991), we obtain new determinations for n_C and n_{L}: $n_C = 820\overset{\circ}{.}1179 \pm 0\overset{\circ}{.}004$ day^{-1} and $n_{\mathrm{L}} = 820\overset{\circ}{.}1502 \pm 0\overset{\circ}{.}004$ day^{-1}. The mean motion of a particle orbiting around Neptune is related to its mean semimajor axis and, if we omit the terms involving the eccentricity and the inclination of the particle (which are both negligible), is expressed as

$$n^2 \sim \frac{GM_{\mathrm{N}}}{a^3} \left(1 + \frac{3}{2} J_2 \frac{R_{\mathrm{N}}^2}{a^2} - \frac{15}{8} J_4 \frac{R_{\mathrm{N}}^4}{a^4} \right) ,$$

where R_{N} is Neptune's equatorial radius, M_{N} is Neptune's mass, and J_2 and J_4 are respectively the planet's second and fourth zonal gravity coefficients (Owen et al. 1991). The determination of the roots of the above equation for the CIR and LR yields $a_C = 62{,}932.41 \pm 0.03$ km and $a_{\mathrm{L}} = 62{,}930.76 \pm 0.03$ km, respectively. Similarly, the revised value for the arc mean motion ($820\overset{\circ}{.}1122 \pm 0.003$ day^{-1}) corresponds to a mean semimajor axis $a_{\mathrm{arcs}} = 62{,}932.70 \pm 0.03$ km. These measurements result in a mismatch $\Delta a_C = 290 \pm 60$ m between the position of the ring arcs and the CIR site, which can be compared with the 250 m half-width of the CIR (Foryta & Sicardy 1996). The new NICMOS astrometric measurements of Galatea and the ring arcs' mean motions show that the arcs are located at the edge of the CIR site, farther from the center of the resonance site than inferred from earlier estimations ($\Delta a_C = 80 \pm 60$ m if we adopt the previously preferred solution, $n_1 = 820\overset{\circ}{.}1194$ day^{-1}, and our revised value for Galatea's mean motion). This calculation confirms both the results based on the analysis of the 1998 October NICMOS data and reported by Dumas et al. (1999), and the results obtained by Sicardy et al. (1999) from adaptive optics observations; that is, while the LR still appears to be responsible for the radial confinement of the ring arcs, as concluded by Porco (1991) from analysis of *Voyager* data, the mismatch between the location of the ring arcs and the center of the CIR suggests that the azimuthal confinement of the arcs cannot be attributed only to the CIR. Other mechanisms have to be counted to explain the azimuthal confinement of the arcs, and alternate models, possibly involving several moonlets co-orbiting with the arcs (Lissauer 1985), should be considered. Namouni & Porco (2001) reported that the 43 : 42 eccentric corotation resonance with Galatea was stronger than the CIR if the arcs were considered to have a small fraction of Galatea's mass. The position of this new resonance would then coincide with the revised NICMOS semimajor axis of the arcs.

Figure 4 represents a comparison between the NICMOS photometric profile of the ring arcs in backscattered light and the *Voyager* profile in forward-scattered light (Porco et al. 1995), after precessing both data sets to epoch 2000 January 1.5 using our revised ring-arc mean motion. This comparison is justified if we consider that *Voyager* reported similar brightness ratios among the three widest arcs at high (forward scattering) and low (backscattering) phase angles. In addition to the position corresponding to mean motion $n = 820\overset{\circ}{.}1122$ day^{-1} (*thick solid line*), we have also represented a slightly different solution for the ring arcs (*thick dashed line*) that was obtained after shifting the previous solution until the highest correlation between the *Voyager* and NICMOS profiles was obtained (the shift of $-2\overset{\circ}{.}3$ is of the same order as the error made in measuring the position of the ring arcs). This new solution corresponds to an arc mean motion of $n = 820\overset{\circ}{.}1116$ day^{-1} ($a_{\mathrm{arcs}} = 62{,}932.73 \pm 0.03$ km), which positions the arcs 320 ± 60 m away from the center of the CIR. Both solutions for the mean motion agree with solution n_2 ($820\overset{\circ}{.}1118$ day^{-1}) determined by Nicholson et al. (1995), and the difference in the revised value of n is mainly due to the difficulty in determining precisely the cen-

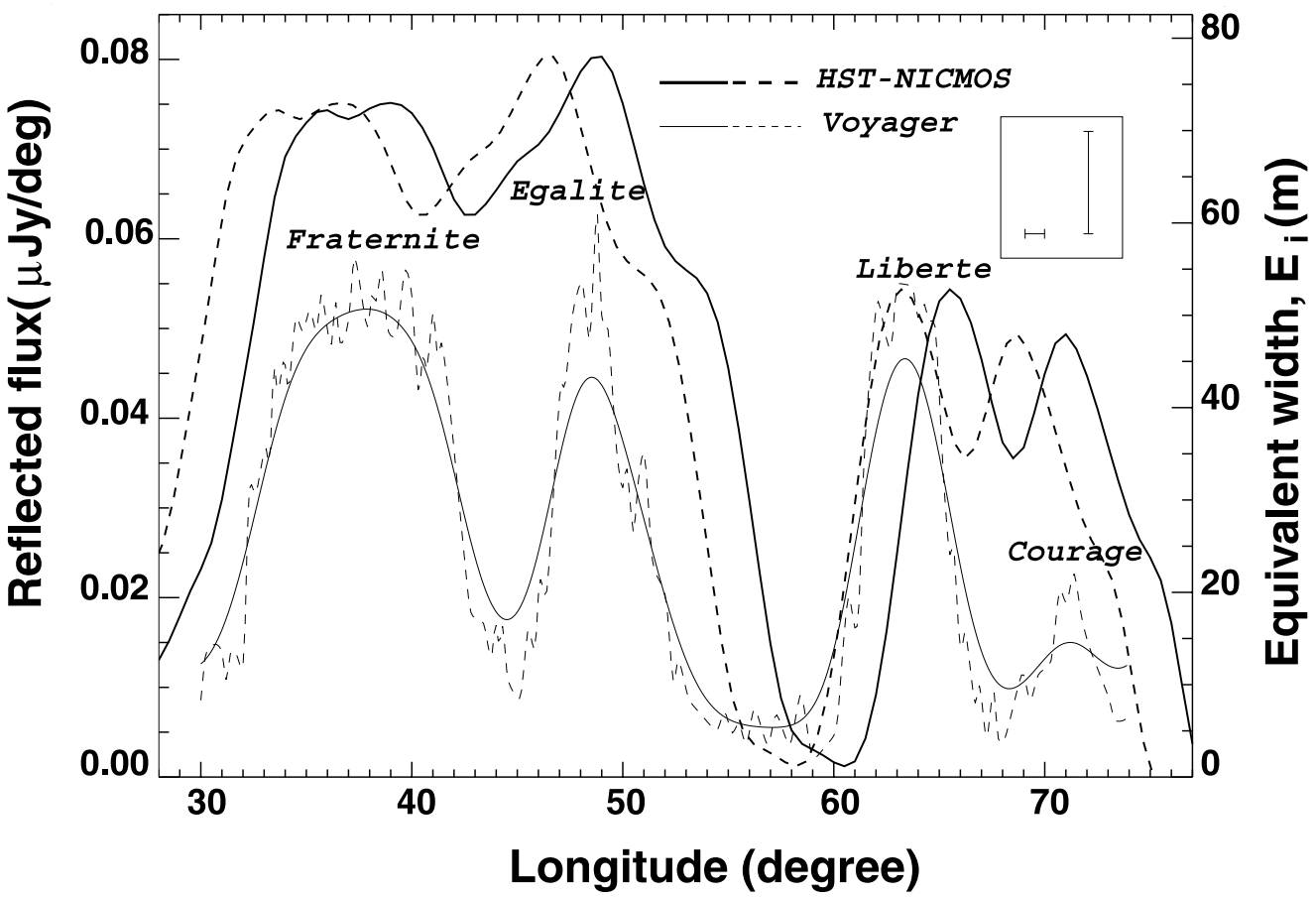

FIG. 4.—Brightness profile of the ring arcs (*thick solid line*) in backscattered light as a function of the orbital longitude (increasing in the direction of motion). The profile is plotted both as the NICMOS radially integrated flux in microjanskys per azimuthal degree and as the equivalent width (E_i) in meters. The ring arcs were precessed to epoch 2000 January 1.5 (JD = 2,451,545.0, Neptune ephemeris time) using our revised arc mean motion, $n = 820.^{\circ}1122\ \mathrm{day}^{-1}$, and longitude is counted from the ascending node of Neptune's equatorial plane on the 2000 Earth equator. The 1989 *Voyager* profile in forward-scattered light (*thin dashed line*), normalized to $E_{i,\mathrm{Egalité}} = 52$ m (Porco et al. 1995), and the convolution of the *Voyager* profile with the NICMOS point-spread function (*thin solid line*) have been precessed to the same epoch with the same mean motion and are overplotted for comparison (the NICMOS uncertainties in the flux and longitude determinations are represented in the inset). Although the main features of the ring arcs appear roughly unchanged since 1989, we note a few differences between the two profiles, particularly for the arcs Liberté and Egalité. Liberté appears to have shifted by $\sim 2^{\circ}$ toward the leading direction, while the width of Egalité has increased. Such changes support the idea that the dust might migrate between adjacent corotation sites (Foryta & Sicardy 1996). A possible solution for the ring arcs' position obtained by maximizing the correlation between the *Voyager* and NICMOS profiles is also represented (*thick dashed line*).

ter of the arc Egalité (Fig. 4 shows that Egalité has become slightly wider since 1989). Also, the ring-arc material displays a reddish color between visible and near-infrared wavelengths, and if we scale both profiles to match the intensity of the trailing arc Fraternité, we note that Liberté has decreased in intensity. If we assume a revised mean motion of $n = 820.^{\circ}1122\ \mathrm{day}^{-1}$, then the positions of Fraternité and Egalité are matched between the two dates, but not the gap between Liberté and the two trailing arcs. Liberté seems to be the only arc whose relative position has changed since 1989, and these changes in morphology and brightness could be the result of transfer of material from Liberté toward Egalité. On the contrary, the solution $n = 820.^{\circ}1116\ \mathrm{day}^{-1}$ better matches the position of Liberté and the gap between leading and trailing arcs, but Egalité and Fraternité appear slightly displaced toward the trailing with respect to their position in 1989.

5. CONCLUSION

The data presented here provide an excellent illustration of the high performance obtained with *HST* and NICMOS for near-infrared observations of small and faint objects of the outer solar system. Additional observations of the Neptunian system at higher spectral resolution are needed to study in more detail the surface composition of the inner moons and ring arcs of Neptune. Higher spatial resolution can also be achieved on large ground-based telescopes equipped with adaptive optics systems and should be used to study the distribution of the material within the arcs. Such programs will return important insights about the dynamical processes involved in maintaining their confinement.

We would like to thank Robert H. Brown for useful discussion and ideas, and Phil Nicholson for his thorough review and the excellent comments he provided to improve the quality of the manuscript, as well as Rodger Thompson and Marcia Rieke from the NICMOS Instrument Definition Team. This work was performed at the Jet Propulsion Laboratory, California Institute of Technology, under contract to the National Aeronautics and Space Administration.

REFERENCES

Akima, H. 1978, ACM Trans. Math. Software, 4, 148
Colas, F., & Buil, C. 1992, A&A, 262, L13
Dumas, C., Terrile, R. J., Smith, B. A., & Schneider, G. 2001, BAAS, 33, 1104
Dumas, C., Terrile, R. J., Smith, B. A., Schneider, G., & Becklin, E. E. 1999, Nature, 400, 733
Dumas, C., Owen, T., & Barucci, M. A. 1998, Icarus, 133, 221
Foryta, D. W., & Sicardy, B. 1996, Icarus, 123, 129
Goldreich, P., Tremaine, S., & Borderies, N. 1986, AJ, 92, 490
Horn, L. J., Hui, J., Lane, A. L., & Colwell, J. E. 1990, Geophys. Res. Lett, 17, 1745
Hubbard, W. B., Brahic, A., Sicardy, B., Elicer, L.-R., Roques, F., & Vilas, F. 1986, Nature, 319, 636
Jacobson, R. A., Lewis, G. D., Owen, W. M., Riedel, J. E., Roth, D. C., Synnott, S. P., & Taylor, A. H. 1990, in A Collection of Technical Papers: AIAA/AHA Astrodynamics Conf. (Washington: AIAA), 157
Karkoschka, E. 1997, Icarus, 125, 348
———. 2001, Icarus, 151, 51
Krist, J. E., & Hook, R. N. 1997, in The 1997 *HST* Calibration Workshop, ed. S. Casertano, R. Jedrzejewski, C. D. Keyes, & M. Stevens (Baltimore: STScI), 192
Labs, D., & Neckel, H. 1968, Z. Astrophys., 69, 1
Lane, A. L., et al. 1989, Science, 246, 1450
Lissauer, J. J. 1985, Nature, 318, 544
Namouni, F., & Porco, C. 2001, BAAS, 33, 1092
Nicholson, P. D., Mosqueira, I., & Matthews, K. 1995, Icarus, 113, 295
Owen, W. M., Vaughan, R. M., & Synnott, S. P. 1991, AJ, 101, 1511
Park, S., & Schowengerdt, R. 1983, Comput. Vision Graphics Image Processing, 23, 258
Pascu, D., et al. 1999, BAAS, 31, 1229
Porco, C. C. 1991, Science, 253, 995
Porco, C. C., Nicholson, P. D., Cuzzi, J. N., Lissauer, J. J., & Esposito, L. W. 1995, in Neptune and Triton, ed. D. P. Cruikshank (Tucson: Univ. Arizona Press), 703
Roddier, F., Roddier, C., Brahic, A., Dumas, C., Graves, J. E., Northcott, M. J., & Owen, T. 1997, Planet. Space Sci., 45, 1031
Sagan, C., & Khare, B. N. 1979, Nature, 277, 102
Sicardy, B., Roddier, F., Roddier, C., Perozzi, E., Graves, J. E., Guyon, O., & Northcott, M. J. 1999, Nature, 400, 731
Smith, B. A., et al. 1989, Science, 246, 1422
Thomas, P., & Veverka, J. 1991, J. Geophys. Res., 96, 19261
Thomas, P., Weitz, C., & Veverka, J. 1989, Icarus, 81, 92
Thompson, R. I., Rieke, M., Schneider, G., Hines, D. C., & Corbin, M. R. 1998, ApJ, 492, L95
Trilling, D. E., & Brown, R. H. 2000, Icarus, 148, 301